J. Electrochem. Sci. Eng. **9(1)** (2019) 55-62; DOI: http://dx.doi.org/10.5599/jese.572

Open Access: ISSN 1847-9286
https://pub.iapchem.org/ojs/index.php/JESE

Original scientific paper

In-situ synthesis of mesoporous carbon/iron sulfide nanocomposite for supercapacitors

Xiaolong Yu, Bogang Li✉

College of Materials Science and Engineering, Sichuan University, Chengdu 610065, China

✉Corresponding author: E-mail libogang@scu.edu.cn

Received: August 7, 2018; Revised: October 20, 2018; Accepted: October 21, 2018

Abstract

Mesoporous C@Fe_xS_y composite as a negative electrode for supercapacitors was synthesized via a one-step hydrothermal treatment followed by an electrodeposition process and its electrochemical properties were studied. Compared with bare carbon sphere, the electrochemical performance of C@Fe_xS_y composite was significantly improved, with a high specific capacitance (267.45 F/g), good rate performance (201.08 F/g at 2.5 A/g), and superior cycling stability (almost no capacitance degradation after 1000 cycles). The results show that the obtained C@Fe_xS_y composite is a promising negative electrode material for supercapacitors.

Keywords

Carbonaceous materials; porous structure; hydrothermal treatment; electrochemical properties; energy storage

Introduction

Supercapacitors have attracted tremendous attention in recent years owing to their high power density, short charging time, and good stability [1–3]. Carbonaceous materials have been widely adopted as negative electrode materials for supercapacitors because of their low cost, good electrical conductivity, and long cycle lifetime. However, carbonaceous materials exhibit limited double-layer capacitance, which limits further development of high energy density supercapacitors [4,5]. One of the effective approaches to enhance the energy density of supercapacitors is to improve the specific capacitance of carbonaceous materials [6–8].

Carbon spheres (CS) with their large surface area, high porosity, and fine pore size is a promising carbonaceous material for supercapacitors. Nevertheless, the low capacitance of CS limits its practical applications [9,10]. To improve the capacitance, researchers have recently focused on developing new negative electrode materials by activation pretreatment, doping modification, and loading of metal-base materials [5,11–13]. Among the metal-base materials, Fe-based materials are

promising candidates because of their suitable working window in negative potential, abundance, low cost, large theoretical capacitance, and nontoxicity [14–17]. Fe-based materials are combined with carbonaceous materials to explore an effective method to prepare composites; this not only could improve the rate performance of Fe-based materials, but also enhance the specific capacitance of carbonaceous materials.

In this work, CS was grown in situ on nickel foam (NF) using a one-step hydrothermal process, and iron sulfide was selected as Fe-based material. A new approach was found to synthesize C@Fe_xS_y composite by using the cyclic voltammetry (CV) electrochemical deposition method to introduce iron sulfide onto CS. The electrical performance of C@Fe_xS_y was investigated, and the results indicated that the C@Fe_xS_y composite exhibited a significantly improved electrochemical performance than bare CS. The findings of this study would open up new possibilities for the design of carbon-based composites for high-performance supercapacitors.

Experimental

Materials

Commercial NF was used as the current collector. Anhydrous dextrose, $FeCl_3 \cdot 6H_2O$, thiourea, and the other reagents in this experiment were used without further purification. Deionized water was used to prepare solutions.

Synthesis of carbon spheres

The CS was prepared by hydrothermal treatment. NF (2×4 cm^2) was treated with hydrochloric acid (3 mol/L), acetone, and absolute ethanol in an ultrasound bath for 10 min, respectively, and then washed with deionized (DI) water. Anhydrous dextrose (10.8 g) was dispersed in 60 ml of DI water and stirred at 25 °C until a clear solution was obtained. The solution was transferred into a 100 ml Teflon-lined autoclave. A piece of NF was placed vertically in the Teflon-lined stainless-steel autoclave, soaked in the solution, at 180 °C for 4 h. Subsequently, CS precursors were formed on the NF. Then, the product was washed with DI water followed by vacuum drying at 60 °C for 12 h and heat treatment at 800 °C for 1 h in a N_2 atmosphere to remove oxygen-containing groups on the surface of the CS.

Synthesis of C@Fe_xS_y composite

C@Fe_xS_y was obtained through an electrochemical deposition method. The experiment was carried out using an electrochemical workstation with a three-electrode cell. CS grown on NF was used as the working electrode, and a platinum plate and a saturated calomel electrode (SCE) were used as the counter electrode and the reference electrode, respectively. $FeCl_3 \cdot 6H_2O$ (1, 1.5, 2, 2.5, and 3 mmol) and thiourea (5 mmol) dissolved in 100 ml DI water was used as the deposition bath. The deposition process was carried out via CV at 5 mV/s for 6 cycles in the voltage range of -1.2 to 0.2 V. The as-prepared C@Fe_xS_y composites with 1, 1.5, 2, 2.5, and 3 mmol of $FeCl_3 \cdot 6H_2O$ are henceforth referred to as C@Fe_xS_y-1, C@Fe_xS_y-1.5, C@Fe_xS_y-2, C@Fe_xS_y-2.5, and C@Fe_xS_y-3, respectively. The as-prepared C@Fe_xS_y-n (n = 1, 1.5, 2, 2.5, and 3) was then carefully rinsed with DI water and dried in a vacuum oven at 60 °C for 12 h.

Characterization and electrochemical measurements

The morphology and the microstructure were observed by scanning electron microscopy (SEM, Hitachi, S-4800). The crystal structure was characterized using an X-ray diffraction (XRD, Rigaku) system with Cu Kα irradiation. The chemical composition of the sample was investigated by X-ray

photoelectron spectroscopy (XPS, ESCALAB 250Xi, Thermo Scientific). The structure of C@Fe_xS_y-2 was further explored by Raman spectroscopy (Renishaw Invia RM200). The Brunauer-Emmett-Teller (BET; Gemini VII) specific surface areas of the samples were determined from N_2 adsorption data in the relative pressure ranging from 0.1 to 1.0.

Electrochemical characterization was carried out using a CHI 660D electrochemical workstation (Chenhua, Shanghai) at 25 °C. The electrochemical characterization includes CV, galvanostatic charge-discharge (GCD), and electrochemical impedance spectroscopy (EIS), using a three-electrode cell with 3.0 M KOH as the electrolyte, materials grown on NF (1×1 cm^2) as the working electrode, Hg/HgO as the reference electrode, and Pt foil as the counter electrode. CV was performed in the voltage window from -1 V to 0 V at scan rates of 5, 10, 20, 30, and 50 mV/s. GCD was carried out between -0.95-0 V at current densities of 0.25, 0.5, 1.0, 1.5, 2.0, and 2.5 A/g. EIS was evaluated in the frequency range of 10^5 to 0.01 Hz. The DC potential and the AC amplitude for EIS measurements are -0.01 V and 5 mV, respectively.

Results and discussion

Morphology and structural analysis

The SEM images of CS and C@Fe_xS_y-2 are presented in Figure 1. Highly dense CSs are distributed on the NF substrate (Figure 1a). These CSs exhibit smooth surfaces and they are connected with each other. This provides high volumetric specific surface area and good mass transport property, which are useful for supercapacitor application. The size distribution of the carbon particles is within the range of 1-2 μm. Figure 1b shows that the C@Fe_xS_y-2 composite maintains the spherical structure, and many Fe_xS_y nanoparticles are dispersed on the surface of the carbon particles. This provides a large surface area for easy diffusion of the electrolyte toward the electrode surface and contributes to the enhancement of specific capacitance.

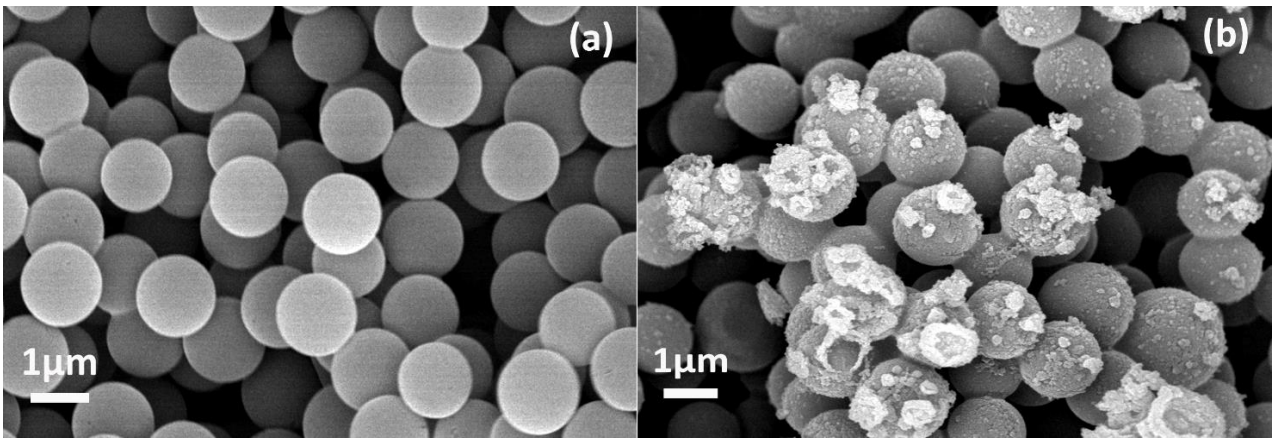

Figure 1. (a) *SEM image of the carbon spheres/NF.* ***(b)*** *SEM image of C@Fe_xS_y-2/NF.*

The XRD patterns of CS and C@Fe_xS_y-2 (Figure 2a) showed similar characteristics. A broad diffraction peak is observed at approximately $2\theta = 23°$ besides peaks of Ni, corresponding to (002) plane of graphitic structure. The decreased peaks for C@FexSy-2 indicate the amorphous nature of Fe_xS_y. Figure 2b shows the Raman spectrum of the CS and C@Fe_xS_y-2 samples. Both of them exhibit two characteristic peaks at 1345 and 1597 cm^{-1}, corresponding to D peak from amorphous structure of carbon and G peak from graphitic structure of carbon, respectively[18,19]. The I_D/I_G ratio of C@Fe_xS_y-2 is 0.97, a little higher than 0.90 of CS, which indicates the C@Fe_xS_y-2 has a small number of defects. The XPS data of C@Fe_xS_y-2 are shown in Figure 2c-d. The peaks at approximately 723 eV

(Fe $2p_{1/2}$), 713 eV (Fe $2p_{3/2}$) and 164 eV in the Fe 2p spectra and the S 2p spectra are assigned to amorphous iron sulfide [20,21]. These results are in good agreement with the SEM observations and further confirm the presence of C@Fe_xS_y-2 on the composite electrode.

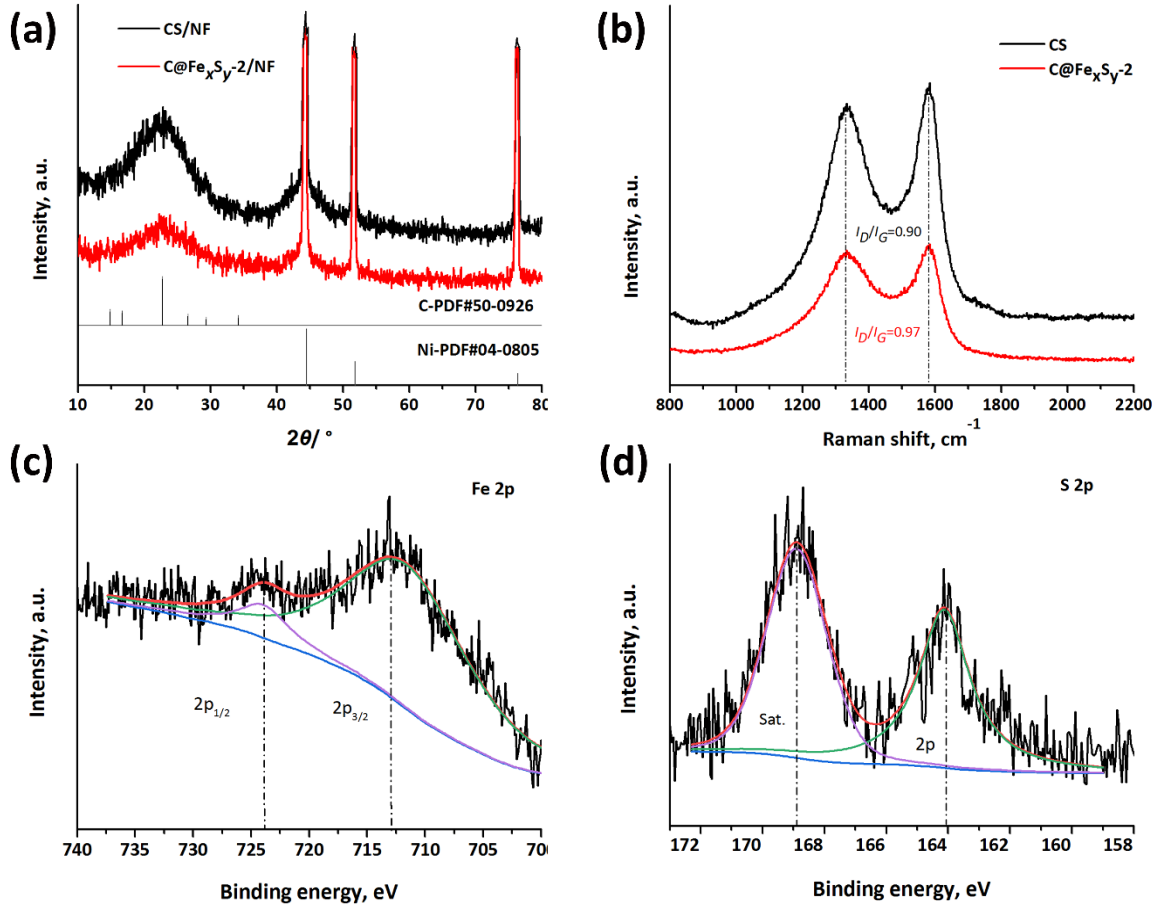

Figure 2. (a) *XRD patterns of CS/NF and C@Fe_xS_y-2/NF electrode.* ***(b)*** *Raman spectra of CS and C@Fe_xS_y-2.* ***(c)-(d)*** *Fe 2p and S 2p XPS spectra of C@Fe_xS_y-2, respectively.*

The nitrogen adsorption-desorption isotherms and Brunauer-Joyner-Halenda (BJH) pore diameter distribution of C@Fe_xS_y-2 are shown in Figure 3. The sample exhibits a typical type IV isotherm and shows a hysteresis loop at medium relative pressure (Figure 3a), which reveals the existence of relatively mesoporous pores. The hysteresis loop exhibits H2 type characteristics, indicating that the sample has a wide pore size distribution. The BET surface area of C@Fe_xS_y-2 is 117.74 m^2/g. The BJH pore diameter distribution of C@Fe_xS_y-2 (Figure 3b) shows that the pore diameter distribution is within the range of 5-10 nm, which further demonstrates that the sample has a mesoporous structure. From the above results, it is evident that the C@Fe_xS_y-2 electrode material has a high specific surface area, and the mesoporous structure could facilitate infiltration of the electrolyte and shorten electron and ion transport distances during energy storage. This would increase the surface utilization of the active material and improve the capacitance of the electrode material.

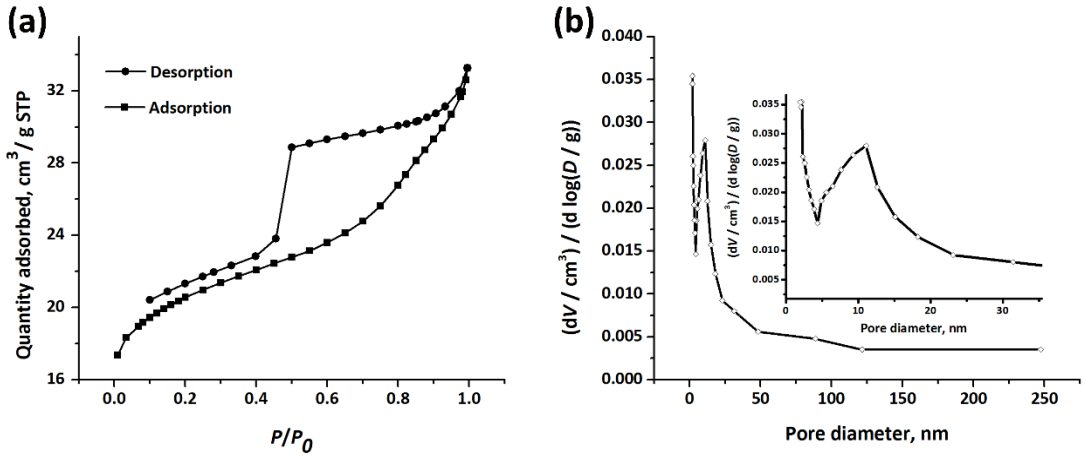

Figure 3. (a) *BET of C@Fe$_x$S$_y$-2.* ***(b)*** *Pore diameter distribution of C@Fe$_x$S$_y$-2.*

Electrochemical performance analysis

The electrochemical performance of the composites was estimated by CV and GCD measurements. Figure 4a shows the GCD curves of CS and C@Fe$_x$S$_y$-n (n = 1, 1.5, 2, 2.5, and 3) at a current density of 0.25 A/g. The charge/discharge curves are nearly linear in shape, indicating ideal electrical double-layer capacitive behavior. The symmetric triangle characteristics reveal the excellent electrochemical reversibility of the samples with high Coulombic efficiency. The C@Fe$_x$S$_y$-2 sample exhibited the longest charge-discharge time, and hence, the largest specific capacitance. The specific capacitance derived from galvanostatic tests can be determined using the following equation [22]:

$$C = \frac{I\Delta t}{m\Delta V} \quad (1)$$

where C is the specific capacitance, I is the discharge current (A), Δt is the discharge time, m is the mass of active materials loaded on the working electrode, and ΔV is the potential window.

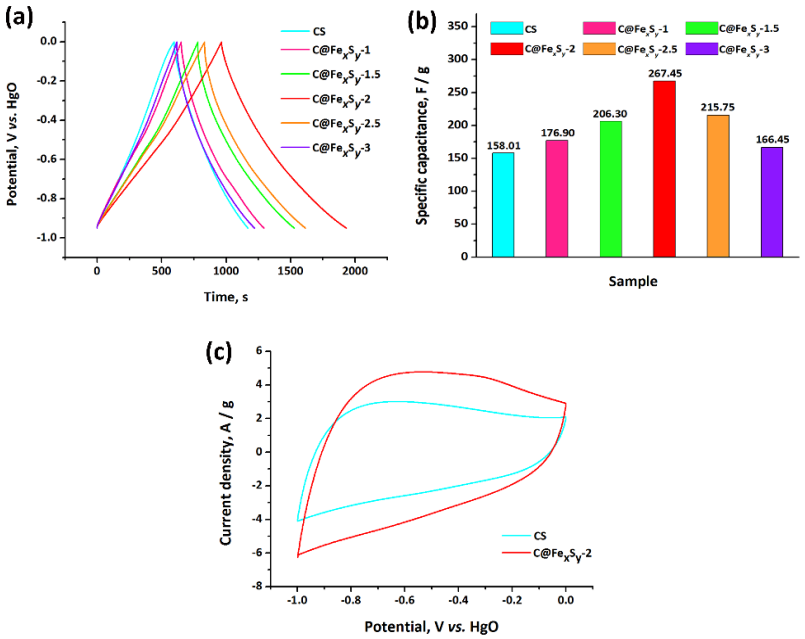

Figure 4. (a) *GCD curves of CS and C@Fe$_x$S$_y$-n (n = 1, 1.5, 2, 2.5, and 3) at a current density of 0.25 A/g.* ***(b)*** *Specific capacitances of CS and C@Fe$_x$S$_y$-n based on the GCD curves.* ***(c)*** *CV curves of CS and C@Fe$_x$S$_y$-2 at a scan rate of 20 mV/s.*

As plotted in Figure 4b, all the C@Fe_xS_y samples exhibit a higher specific capacitance than the CS electrode (158.01 F/g); C@Fe_xS_y-2 has the highest specific capacitance of 267.45 F/g at 0.25 A/g. It is considered that the loading mass of Fe_xS_y affected the capacitance, and C@Fe_xS_y-2 has the optimum loading mass. The reason might be that Fe_xS_y deposited on the surface of CS provides a porous structure, which further increases the specific surface area of the electrode material and thus enhances the capacitance. However, owing to the poor conductivity of Fe-base materials, when the loading mass of Fe_xS_y further increases, the capacitance of the electrode material decreases. Figure 4c shows the CV curves of CS and C@Fe_xS_y-2 at a scan rate of 20 mV/s. As expected, the C@Fe_xS_y-2 composite shows a much higher capacitance than CS.

The electrochemical performance of C@Fe_xS_y-2 for supercapacitor applications was investigated in KOH solution with a three-electrode system. As shown in Figure 5a, CV test was carried out at various scan rates of 5-50 mV/s. The quasi-rectangular shape of the CV curves with an obvious hump shape indicates the effect of electrical double-layer capacitance. Moreover, the rectangular shape of the curve even at a high scan rate of 50 mV/s suggests the outstanding capacitive behavior and high ionic conductivity of C@Fe_xS_y-2. The inconspicuous redox peaks may be induced by Fe_xS_y. These results demonstrate that C@Fe_xS_y-2 provides numerous accessible pores and paths for ion transfer. Figure 5b-c show the discharge curves of C@Fe_xS_y-2 and CS at different current densities. All the curves exhibited excellent linear response, implying the ideal electric double-layer capacitive behavior of the samples. It is evident from Figure 5d that C@Fe_xS_y-2 has a much higher capacitance than CS at all current densities. Remarkably, the C@Fe_xS_y-2 electrode exhibited capacitance retention of 75 % when the current density was increased from 0.25 to 2.5 A/g, indicating its outstanding rate capability.

The cycling stability of C@Fe_xS_y-2 was evaluated for 1000 cycles at a high charging-discharging current density of 2.5 A/g. As shown in Figure 5e, the C@Fe_xS_y-2 electrode does not show capacitance degradation, and the charge/discharge curves in the last ten cycles are almost identical to those in the first ten cycles. After 1000 cycles, the capacitance retention of the C@Fe_xS_y-2 electrode is even 103 % of the initial capacitance, indicating its superior cyclic performance. The reason for the slight increase in the capacitance may be the gradual entry of the electrolyte into the inner micropores of the C@Fe_xS_y-2 electrode after several cycles, which increases the contact area of the electrode and electrolyte, thus enhancing the capacitance.

EIS was used to gain a deep understanding of the rate capability of the C@Fe_xS_y-2 electrode. Figure 5f shows the Nyquist plots of C@Fe_xS_y-2 and CS. It can be seen that the Nyquist plot is mainly composed of two parts: a semicircle in the high frequency range and a vertical line in the low frequency region. The inset in Figure 5f shows the magnified portion of the Nyquist plot near the origin, providing more details on the electrode impedance behavior. The *x*-intercept of the high frequency semicircle provides the value of equivalent series resistance (R_s) of the electrochemical system [23,24]. It is observed that the R_s values of C@Fe_xS_y-2 and CS are 0.60 and 0.71 Ω, respectively. The diameter of the high frequency semicircle corresponds to the charge transfer resistance (R_{ct}). The R_{ct} of C@Fe_xS_y-2 and CS was calculated to be 0.12 and 0.50 Ω, respectively. As for C@Fe_xS_y-2, the low resistances are associated with Fe_xS_y nanoparticles on the carbon substrate, which provide a larger electrolyte/electrode interface, facilitating the electrode material wetting and the ion transfer. The Nyquist plot of C@Fe_xS_y-2 exhibits an obvious Warburg 45° line region, corresponding to the semi-infinite ion diffusion resistance, which reflects a lower ion diffusion rate within the porous C@Fe_xS_y-2 electrode [25,26]. In the low-frequency region, the straight line represents the good capacitive behavior of the electrode and the more parallel to the virtual axis,

the closer to the double-layer capacitance [27]. The Nyquist plot in the low frequency range of C@Fe_xS_y-2 shows a less vertical line, which is an indication that C@Fe_xS_y-2 has diffusion-controlled faradaic processes due to the higher contribution of Warburg impedance [28-30].

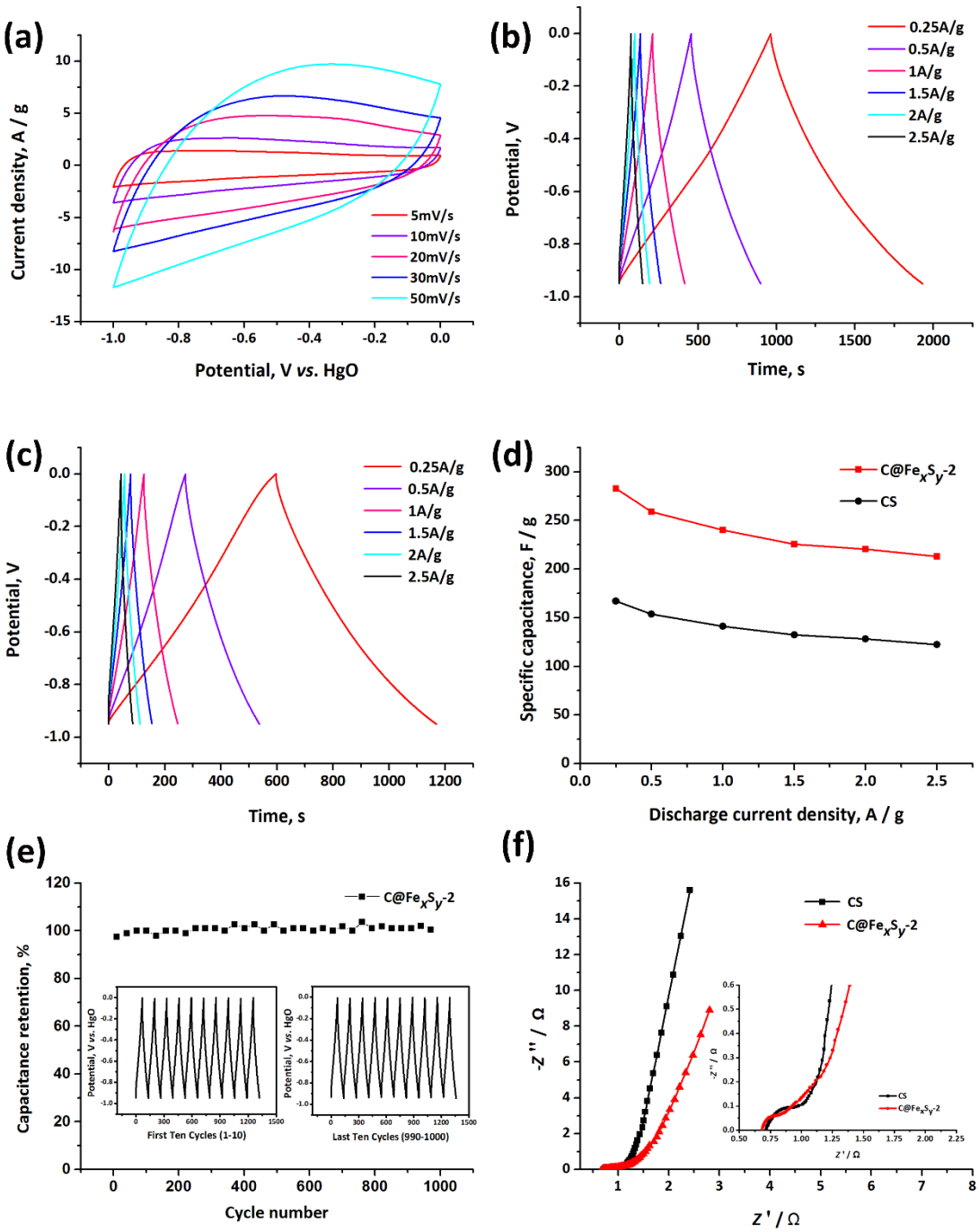

Figure 5. (a) *CV curves of C@Fe_xS_y-2 at different scan rates.* ***(b)-(c)*** *GCD curves of C@Fe_xS_y-2 and CS at different current densities, respectively.* ***(d)*** *Specific capacitance of C@Fe_xS_y-2 and CS at different discharge current densities.* ***(e)*** *Cycling performance of the C@Fe_xS_y-2 electrode at a current density of 2.5 A/g.* ***(f)*** *Electrochemical impedance spectra of C@FexSy-2 and CS.*

Conclusions

In this study, a mesoporous negative electrode C@Fe_xS_y composite was successfully fabricated on NF using a hydrothermal method followed by an electrodeposition treatment. The electrochemical performance of the C@Fe_xS_y-2 electrode was significantly higher than that of bare

CS. The hybrid electrode demonstrated a high specific capacitance (up to 267.45 F/g), good rate performance (201.08 F/g at 2.5 A/g), and superior cycling stability (almost no capacitance degradation after 1000 cycles). The excellent electrochemical behavior could be attributed to the unique hybrid electrode design and the enhancement in the surface area. The present study provides an adaptable method for novel design of negative electrode materials for supercapacitors, extending the potential applications of carbon-based devices.

***Acknowledgements**: The authors greatly appreciate the support of Xinyue Huang, Xingye Tong, and Xiaoming Tu.*

References

[1] X. Yuan, B. Tang, Y. Sui, S. Huang, J. Qi, Y. Pu, F. Wei, Y. He, Q. Meng, P. Cao, *Journal of Materials Science: Materials in Electronics* **3** (2018) 1-13.
[2] P. Simon, Y. Gogotsi, *Nature Materials* **7** (2008) 845-854.
[3] S. Liu, L. Wang, C. Zheng, C. Qidi, M. Feng, Y. Yu, *ACS Sustainable Chemistry & Engineering* **5** (2017) 9903-9913.
[4] B. Lv, P. Li, Y. Liu, S. Lin, B. Gao, B.-Z. Lin, *Applied Surface Science* **437** (2017) 169-175.
[5] N. Syarif, IA. Tribidasari, W. Wibowo, *Journal of Electrochemical Science & Engineering* **3(2)** (2013) 37-45.
[6] H. Zhang, X. Zhang, Y. Ma, *Electrochimica Acta* **184** (2015) 347-355.
[7] X. Yang, H. Ma, G. Zhang, *Langmuir : The ACS Journal of Surfaces and Colloids* **33** (2017) 3975-3981.
[8] J. Pang, W. Zhang, H. Zhang, J. Zhang, H. Zhang, G. Cao, M. Han, Y. Yang, *Carbon* **132** (2018) 280-293.
[9] T. Liu, L. Zhang, W. You, J. Yu, *Small* **14** (2018) 1702407.
[10] J.-G. Wang, H. Liu, H. Sun, W. Hua, H. Wang, X. Liu, B. Wei, *Carbon* **127** (2017) 85-92.
[11] D. Iglesias, E. Senokos, B. Aleman, L. Cabana, C. Navío, R. Marcilla, M. Prato, J. J. Vilatela, S. Marchesan, *ACS Applied Materials & Interfaces* **10** (2018) 5760-5770.
[12] X. Xia, Y. Zhang, Z. Fan, D. Chao, Q. Xiong, J. Tu, H. Zhang, H. Jin Fan, Y. X Xia, D. Zhang, J. Chao, Fan, Q. X Xia, J. Xiong, Tu, Z. H Fan, Zhang, *Advanced Energy Materials* **5** (2014) 1-9.
[13] J. Tang, J. Wang, L. Shrestha, S. Hossain, Z. Alothman, Y. Yamauchi, K. Ariga, *ACS Applied Materials & Interfaces* **9** (2017) 18986-18993.
[14] J. Ma, X. Guo, Y. Yan, H. Xue, H. Pang, *Advanced Science* **5** (2018) 1700986.
[15] Y. Zhang, R. Lin, Y. Fu, X. Wang, X. Yu, J. Li, Y. Zhu, S. Tan, Z. Wang, *Materials Letters* (2018) 9-12.
[16] Y. Zhong, J. Liu, Z. Lu, H. Xia, *Materials Letters* **166** (2015) 223-226.
[17] M.A. Azam, R.N.A.R. Seman, M.A. Mohamed, *Advances in Natural Sciences: Nanoscience and Nanotechnology* **7(4)** (2017) 1-10.
[18] J. Wu, H. Xu, J. Zhang, *Acta Chimica Sinica* **72(3)** (2014) 301-318.
[19] T. Jawhari, A. Roid, J. Casado, *Carbon* **33(11)** (1995) 1561-1565.
[20] J. Feng, L.T. Peckler, A.J. Muscat, *Crystal Growth & Design* **15** (2015) 3565-3572.
[21] V. Sridhar, H. Park, *Journal of Alloys and Compounds* **732** (2017) 799-805.
[22] N. Zhang, C. Fu, D. Liu, Y. Li, H. Zhou, Y. Kuang, *Electrochimica Acta* **210** (2016) 804-811.
[23] J.-G. Wang, Y. Yang, Z.-H. Huang, F. Kang, *Carbon* **61** (2013) 190-199.
[24] H. Yoo, J. Hyun Jang, J. Heon Ryu, Y. Park, S. M. Oh, *Journal of Power Sources* **267** (2014) 411-420.
[25] J.-G. Wang, Z. Zhang, X. Zhang, X. Yin, X. Li, X. Liu, F. Kang, B. Wei, *Nano Energy* **39** (2017) 647-653.
[26] J. Gao, X. Wang, Y. Zhang, J. Liu, Q. Lu, M. Liu, *Electrochimica Acta* **207** (2016) 266-274.
[27] W. Zhang, C. Xu, C. Ma, G. Li, Y. Wang, K. Zhang, F. Li, C. Liu, *Advanced Materials* **29(36)** (2017) 1701677.
[28] M.R. Lukatskaya, B. Dunn, Y. Gogotsi, *Nature Communications* **7** (2016) 12647.
[29] J. Liu, J. Wang, C. Xu, H. Jiang, C. Li, L. Zhang, *Advanced Science* **5(1)** (2018) 1700322.
[30] X. Du, C. Wang, M. Chen, Y. Jiao, *The Journal of Physical Chemistry C* **113(6)** (2009) 2643-2646.